Iraqi Journal of Physics, 2024 *Vol. 22, No. 2, PP. 31-47*
https://doi.org/10.30723/ijp.v22i2.1204 *P-ISSN: 2070-4003*
E-ISSN: 2664-5548

Two-Step Laser Ablation for the Synthesis of Au:Pb Core/Shell NPs for a High-Performance Silicon-Based Heterojunction Photodetector

Zeina A. Abdul Hameed[1a] and Falah A-H. Mutlak[1b*]
[1]*Department of Physics, College of Science, University of Baghdad, Baghdad, Iraq*
[b]E-mail: zeina3461@gmail.com
[a*]Corresponding author: falah.mutlak@sc.uobaghdad.edu.iq

Abstract

In this work, colloidal gold:lead (Au:Pb) core/shell nanoparticles (NPs) were synthesized in liquid at 532 nm using the laser ablation method. An investigation of the external magnetic field during the laser ablation process affected the properties of the Au:Pb NP core and shell. The magnetic field enhances the core shell's crystallinity. The optical band gap energy increased from 2.067 to 2.086 eV in the presence of the magnetic field. It also led to an increase in the concentration and a decrease in the size of nanoparticles, which led to increased absorbance. A magnetic field strength of 250 mT resulted in a higher removal efficiency. The external magnetic field significantly reduced NP agglomeration and aggregation. We created and characterized an Au:Pb/porous silicon (PS) heterojunction photodetector. The magnetic field greatly enhanced its properties. The responsively (R_λ) of the photodetector increased from 0.093 to 0.551 A/W at λ = 650 nm by increasing the magnetic field. On the other hand, the final Au:Pb/PS material had the best photocurrent stability, demonstrating that adding Au:Pb NPs can make PS's opto-electrical properties more stable. In the end, the Au:Pb NPs/PS heterojunction photodetector results showed that the photodetector parameters got much better when a magnetic field was present. By altering the preparation conditions, we can produce high-performance core/shell photovoltaic devices.

Article Info.

Keywords:
Si Nanostructure, Laser Ablation, Au:Pb NPs, Photodetector, Electrochemical Etching.

Article history:
Received: Sep. 18, 2023
Revised: Oct. 25, 2024
Accepted: Jan. 08, 2024
Published: Jun. 01,2024

1. Introduction

The application of nanotechnology and nanoparticles has expanded too many fields. Bulk materials often lack the many characteristics that nanoparticles possess [1]. Nanoparticles' size, shape, and composition greatly affect their electrical, optical, and magnetic characteristics [2]. Gold nanoparticles (AuNPs) are an intriguing nanomaterial that has various applications in fundamental sciences [3, 4]. Many procedures, such as laser ablation, physical irradiation, chemistry, electrochemistry, and biological procedures, involving plants and bacteria can be used to synthesize AuNPs [5, 6]. AuNPs were utilized with single electron devices as well as scanning laser microscopy to study cellular processes [7, 8].

Thus, researchers have looked into the luminescence [9, 10] and sensing capacities [11, 12] of mixtures of metal nanoparticles and porous silicon. Surfaces of porous silicon (PS) substrates coated with noble metal nanoparticles, to enhance Raman scattering, have also been the subject of much research [13, 14]. On polished Si surfaces, the hydrodynamic disturbance caused by changes in thin-film thicknesses and vacancies is insensitive to differences in substrate topography [15, 16]. Metallic nanoparticles exhibit surface plasmon resonance (SPR), an essential optical property. Light's electromagnetic radiation causes electrons in a conductor to oscillate collectively, leading to Surface Plasmon Resonance [17]. Self-assembling nanomaterials, photovoltaics, and nonlinear optics are all products of catalysis [18, 19]. Some applications of nanoscale materials include chemical and biological processes as

well as optomechanical sensors [20, 21]. Recent studies [22, 23] suggest that nanoparticles might be produced by liquid laser ablation. It is an innovative method with many potential uses. Because of their versatility [24, 25], AuNPs have been studied and used in many different fields [26, 27]. Their absorption is affected by the chemical surroundings, AuNPs' diameter, and electrical insulator's core [28, 29]. Due to the proximity of the valence band and conduction band, electron transport in AuNPs is straightforward. SPR occurs when the electron amplitude of a nanoparticle resonates with an optical wave [30, 31]. Metals, oxides, alloys, and semiconductor nanoparticles are just some of the many materials created using the Pulsed Laser-Ablation in Liquids (PLAL) [32, 33].

There is a wide variety of lead nanoparticles (PbNPs) applications in industry [34, 35]. The tiny size of lead nanoparticles makes them behave differently from the bulk material [36]. Physical, chemical, and biological methods can all be used to produce lead nanoparticles. In this study, PbNPs were synthesized using laser ablation of compressed lead metal. Colloids are spherical NPs produced by laser ablating of metal oxides and pure metals in water. The morphologies of the produced nanoparticles vary greatly with temperature [37].

In this study, Au:Pb core/shell NPs were synthesized by laser ablation, with a magnetic field of different strength applied during the production of the NPs. Optical and electrical characteristics, in addition to the structure of the prepared NPs, were investigated. Au:Pb NPs core/shell onto porous silicon were used to develop an ultra-high-sensitive photodetector, and its characteristics were studied.

2. Experimental

Colloidal Au:Pb core/shell NPs were created using a Q-switched Nd:YAG laser with a pulse duration of 9 ns and a wavelength of 532 nm. An Au target in the bottom of a glass vessel containing distilled water was hit with a focused Nd:YAG laser of 500 pulses to produce colloidal Au nanoparticles. To create Au:Pb core/shell nanoparticles, a Pb target was hit with a 1020 mJ laser and 300 pulses in the glass jar containing the colloidal Au nanoparticles. This was done under the influence of an external magnetic field. For this purpose, an electromagnet of two coils encircled the glass vessel in a direction that is perpendicular to the laser plume's direction, as shown in Fig. 1 (a). Each coil had 1000 turns and 22 layers of copper wires with a radius of 0.5 mm. It was attached to a nickel spherical (10 mm in radius) pole with a hole in the center. The coils were 65 m long, and the hole's diameter was 5 mm. The electromagnetic electrical circuit comprised a 4 rev/min reduction gearbox, a 220 V rotator motor, a capacitor (1000 F at 400 V), and a 0-220 V variac. The applied magnetic field strength ranged from 40 mT to 250 mT.

A UV–Vis double beam spectrophotometer was used to analyze the optical absorption of colloidal Au:Pb core/shell nanoparticles. An X-ray diffractometer was used to analyze the structural characteristics of the nanoparticles. Transmission electron microscope (TEM) was used to investigate the shape and particle size of the synthesized core/shell nanoparticles. The composition of the Au:Pb core/shell nanoparticles was evaluated with a scanning electron microscope (SEM).

A photodetector was fabricated using the Au:Pb core/shell nanoparticles. The photodetector's substrate was a 1 cm^2 patch of mirror-like p-type silicon with (100) orientation and a 0.1–100-Ω.cm electrical resistance. The silicon substrates were washed with distilled water before being etched using diluted hydrofluoric acid (HF) to remove the natural oxide from the silicon's outermost layer. After cleaning, a thin layer of Au:Pb core/shell NPs was deposited on the silicon substrate using the spin coating technique. The Au:Pb core/shell NPs film on the back side of the silicon substrate was

coated with In and Al films using the thermal resistive technique, as shown in Fig. 1 (b), to create electrodes, which were connected to external devices using silver paste. At room temperature, measurements of the Au:Pb NPs/PS heterojunction's current-voltage characteristics were made in the dark and under illumination. The photodetector's spectral working range, spectral responsiveness, and specific detectivity are among its key strengths.

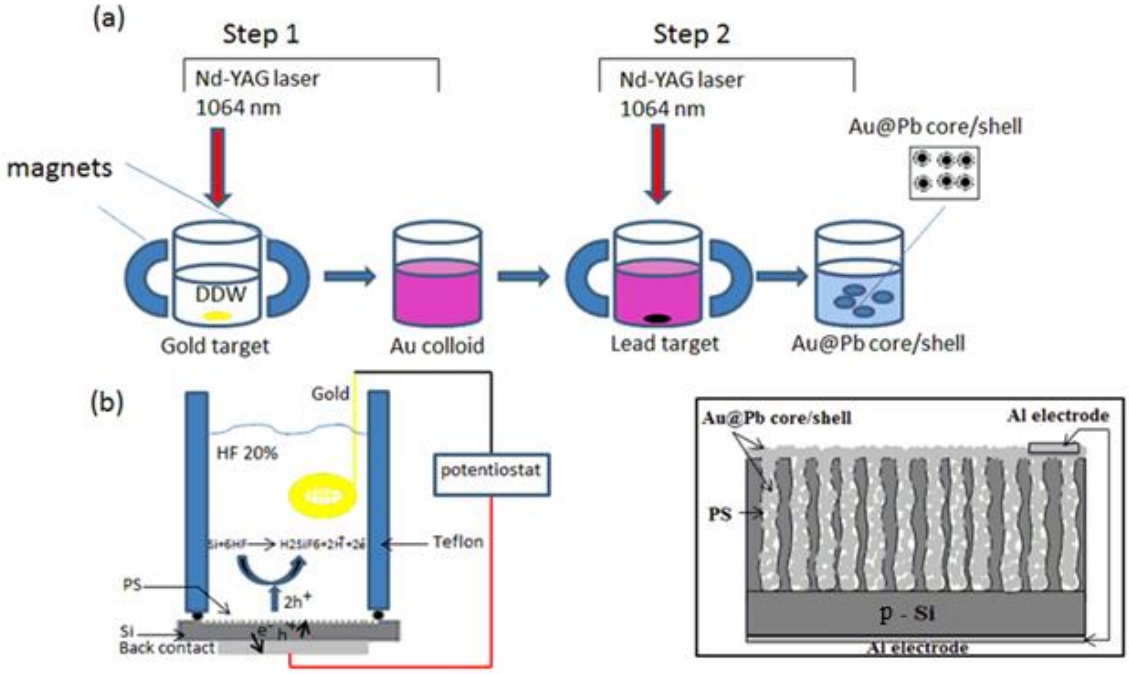

Figure 1: (a) Experimental frame-work of the PLAL assisted by a magnetic field and (b) detailed working diagram of the electrochemical etching method.

3. Results and Discussion

Fig.2 (a-e) presents the XRD patterns of the Au:Pb core/shell NPs. Six peaks were noted for PbNPs that correspond to the planes (111), (200), and (222) at $2\theta = 31.3^{o}$, 52.3^{o}, and 65.3^{o}, respectively. Also, planes (111), (200), and (311) at $2\theta = 38.1^{o}$, 44.3^{o}, and 77.7^{o}, respectively, overlap with PS (100). It was demonstrated that the core/shell synthesis process can be enhanced by applying an external magnetic field. Intensifying the magnetic field for a longer period of time appears to induce the collapse of the plasma cloud, leading to a greater concentration of ablated nanoparticles. The use of the liquid laser ablation with magnetic field support may be can reduce the Van der Waals-induced particle aggregation. This weakening is caused by charged particles colliding with the higher plasma frequencies. When a magnetic field is applied, magnetic NPs like Pb are subject to Van der Waals, dipole-field, and dipolar interaction forces.

Magnetically charged particles interacting with Pb nanoparticles, which have high surface energy, provide the initial force. The third force [38, 39] keeps the nanoparticles' magnetic momentum perpendicular to the magnetic field's steady state. It is possible that the third force might assist in increasing the crystallinity of the manufactured nanoparticles.

Scherrer equation, Eq. 1, can be used to calculate the mean crystallite size (D) of the Au:PbNPs when an applied magnetic field (B) of 250 mT is employed:

$$D = \frac{0.9\,\lambda}{\cos\theta\ FWHM} \qquad (1)$$

Table 1 shows the data extracted from the X-ray diffraction patterns of Au:Pb NPs/PS powder synthesized by laser ablation at 532nm and a magnetic field of 250 mT.

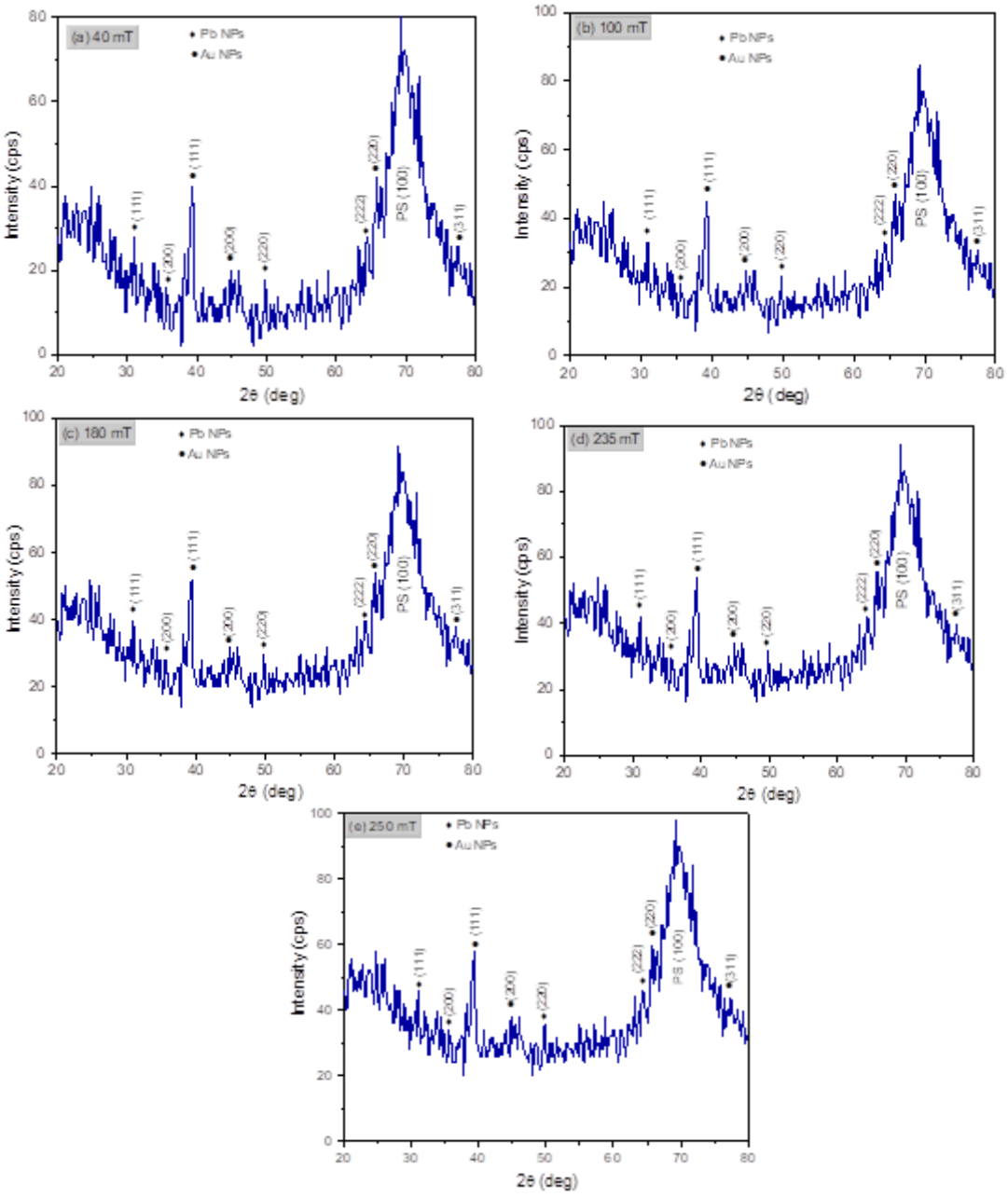

Figure 2: XRD patterns of Au:Pb NPs/ PS synthesized by laser ablation at different magnetic fields.

Table 1: The XRD diffraction values for Au:Pb NPs/PS synthesized by laser ablation at laser wavelength of 532 nm with 250 mT magnetic field.

Sample	Miller indices	2 theta (deg)	FWHM (deg)	d_{hkl} (A^0)	D (nm)
Pb NPs	(111)	31.3	1.7	2.9	4.86
	(200)	36.3	1.59	1.3	4.9
	(220)	52.3	1.56	1.7	5.72
	(222)	65.3	1.57	1.4	6.02
Au NPs	(111)	38.2	1.90	2.4	4.4
	(200)	44.3	1.70	2.08	5.08
	(220)	64.5	1.60	1.44	5.9
	(311)	77.7	1.58	1.24	4.86

According to Fig.3, magnetically ablated colloidal Au:PbNPs (core/shell) have UV-Visible absorption spectra. As a result of the smaller colloidal NPs and increased concentration of NPs produced with the magnetic field, the optical absorbance of Au:PbNPs core/shell was high. The inset of Fig. 3 illustrates the proof supporting this conclusion. Yet, when NPs have numerous holes, the size of particles may increase. As the magnetic field strength increased, the absorbance peak at 500–550 nm shifted towards the blue wavelength. This shift is due to the small size of the NPs. Fig. 3 demonstrates that the absorbance decreased as the magnetic field strength was increased, specifying less efficient laser ablation. At the same time, disorder was introduced into the plasma formation process when the magnetic field strength was more than 180 mT, which caused specific granules to de-merge and prevent (SPR).

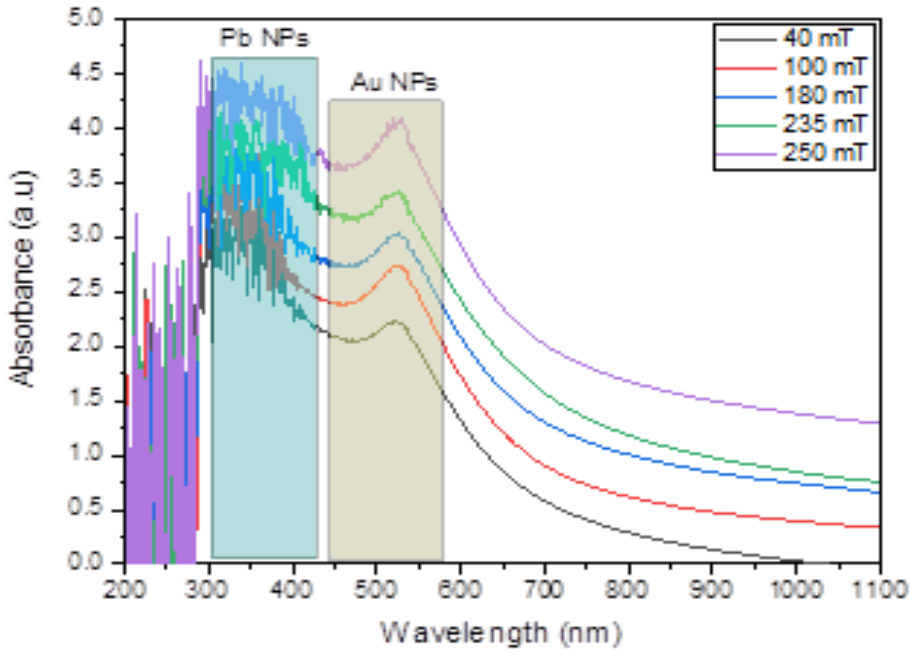

Figure 3: Absorption parameters of the Au:PbNPs colloidal solution prepared with the use of different magnetic fields.

Fig.4 (a) shows TEM images of Au:Pb NPS synthesized with no magnetic field; spherical particles of different sizes were noted. The core/shell structure was confirmed by higher magnification of TEM images, which showed a core diameter of 60 nm and a mean shell thickness of 20 nm. Fig.4 (b) illustrates how adding external M-field

(250mT) increased concentration of the NPs and caused a linear chain-like structure to form. This chain arrangement of the Au:Pb NPs is due to their Ferro-magnetic properties, which caused the core to get smaller; the nanoparticles core diameter decreased to 45 nm and the shell thickness to 18 nm.

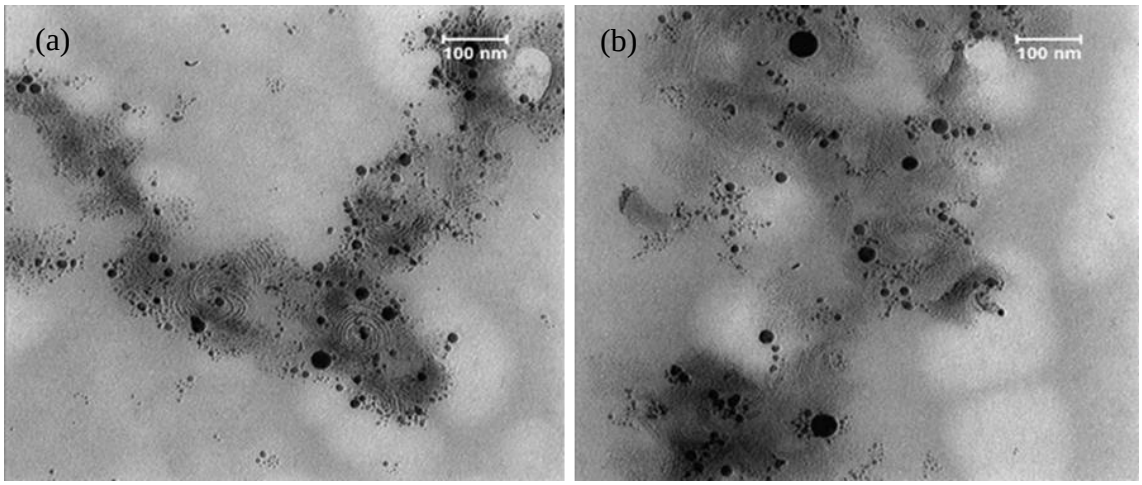

Figure 4: TEM images of Au:PbNPs prepared with (a) no magnetic field, (b) B = 250mT.

The diameter of Au:Pb nanosheets was noted to change over time, as seen in the SEM images, as shown in Fig.5. The development of nanosheets accompanied the finding of additional spherical NPs. This may be due to the quick cooling and heating that took place throughout laser ablation; smaller particle size resulted from the stronger magnetic field. The product morphology is consistent with a core-shell structure. With the external magnetic field, Au:PbNPS became more stable and less likely to group together to create larger aggregates.

Fig.6 depicts the Au:PbNPs/PS photoluminescence (PL) spectra. The effect of the quantum confinement widened the energy gap in the samples synthesized with the magnetic field applied throughout the laser ablation. Additionally, Au:PbNPs/PS PL spectra excitation was at 589 nm and exhibited a band gap red shift. Au:PbNPs' nano-scale structure was enhanced by this alteration. According to TEM measurements, the small size of Au:PbNPs appears to be the cause for the band gap energy increase occurring when applying the magnetic field. Even though Au:PbNPs PL spectra behavior as a size function seems to be divided into two trends, the quantum confinement theory is supported by energy decline with the size that was observed in the two instances. Those two patterns have previously been observed with the presence of the magnetic field. Table 2 displays the band gap energy of Au:PbNPs synthesized with different external magnetic field strengths. Au:PbNPs/PS band gap energy produced with a 250mT magnetic field was greater than that synthesized with 40 mT due to the small size of the particles produced with the higher magnetic field strength.

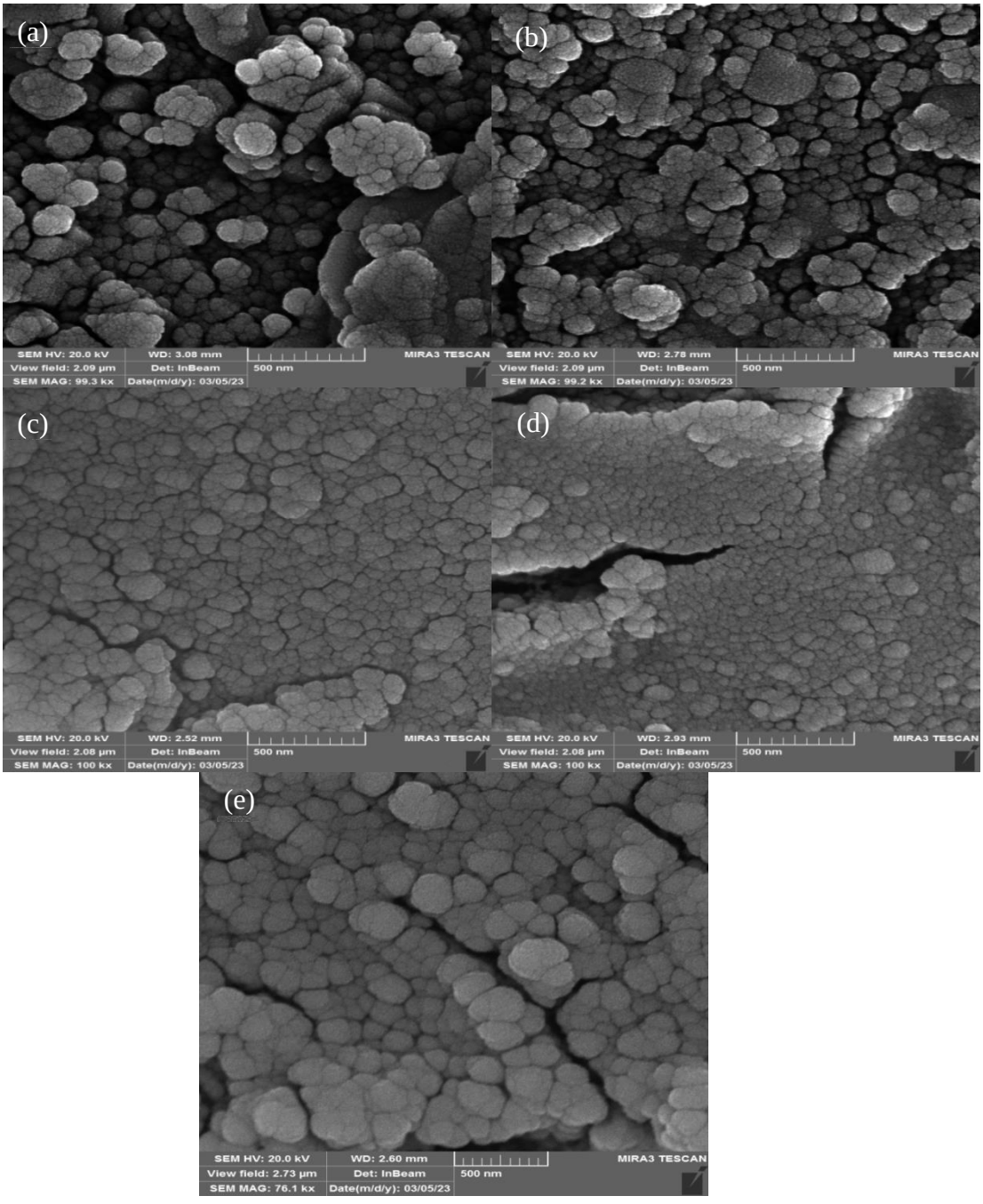

Figure 5: SEM images of Au:PbNPS synthesized with various magnetic field strength of (a) B = 40 T, (b) B = 100 mT, (c) B = 180 mT, (d) B = 235mT and (e)B=250mT.

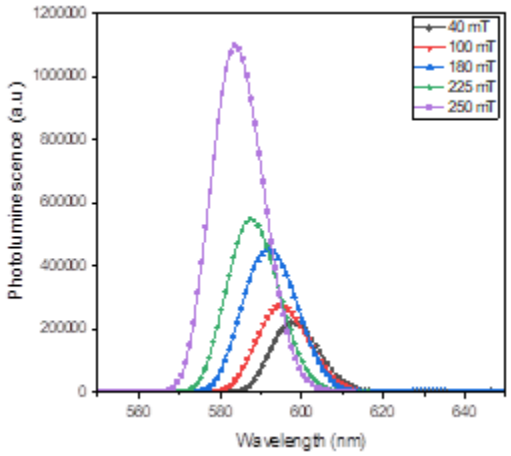

Figure 6: Photoluminescence spectra of Au:Pb NPs/ PS synthesized by the laser ablation with different magnetic fields.

Table 2: Values acquired from PL spectra peaks of Au:PbNPS/PS with different magnetic fields.

Magnetic field (mT)	λ max (nm)	E_g (eV)	FWHM (nm)
40	599.7	2.067	21.79
100	597.9	2.073	19.99
180	597.9	2.073	16.38
235	596.1	2.079	23.79
250	594.3	2.086	18.98

In the region of (1005-1500 cm^{-1}), the Raman spectra of the Au:PbNPs core-shell /PS recorded for all of the samples produced with various magnetic field strengths show the presence of two modes, as shown in Fig. 7. The results of this study complement those of prior studies [40, 41], showing that the phonon modes observed in Raman spectra of synthetic materials are congruent with the specified vibration modes for PS. The peak intensity rises with the increase of the magnetic field strength because there are more core-shell nanoparticles. Adding a magnetic field is highly important in boosting the Raman intensity, since it strengthens Raman peaks.

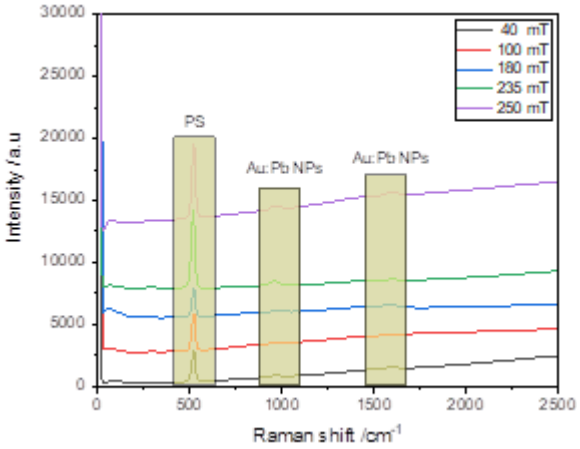

Figure 7: Raman spectra the of Au:PbNPs/PS.

Fig. 8 shows forward and reverse bias J-V curves for the Au:PbNPs/PS in the dark in the voltage range (+5 V To -5 V). An increase in magnetic field strength results in a higher current in the Au:PbNPs/PS sample. A very noticeable increase of current is seen with B=250mT, indicating that the magnetic field contributed to the Au:PbNPs/PS's high level of conductivity. This means that the resistance drops with increasing output current.

Barrier height ($\emptyset_{Bn}$) and ideality factor (n), as listed in Table 3, for the sandwich structure of Al/Au:PbNPs/PS/Al were determined from the J-V curves according to the following equations:

$$\emptyset_{Bn} = \frac{K_B\, T}{q}\, ln\left(\frac{A^{**}\, T^2}{J}\right) \qquad (\mathbf{2})$$

where: V is the applied voltage, (J) (mA/cm^2) is the forward current density, (k_B) (=1.38x10^{-23}J/K) is Boltzmann constant, and (A**) is Richardson constant (=32A/cm^{2}K^2 for P-type silicon).

$$n = \frac{q}{k_B\, T}\frac{dv}{d(lnJ)} \qquad (\mathbf{3})$$

Bias voltage regarding Al/Au:PbNPs/PS/Al is equally distributed across the structure; however, the streaming crossover current isn't. A lot of interactions are expected between excited electrons and holes since they lack the energy needed for passing the barrier. Heterojunctions created by a magnetic field have a lower value of (n) because they have less surface states and particle aggregation at the interface and more electrical conductivity in Au:Pb/PS, as illustrated in Table 3.

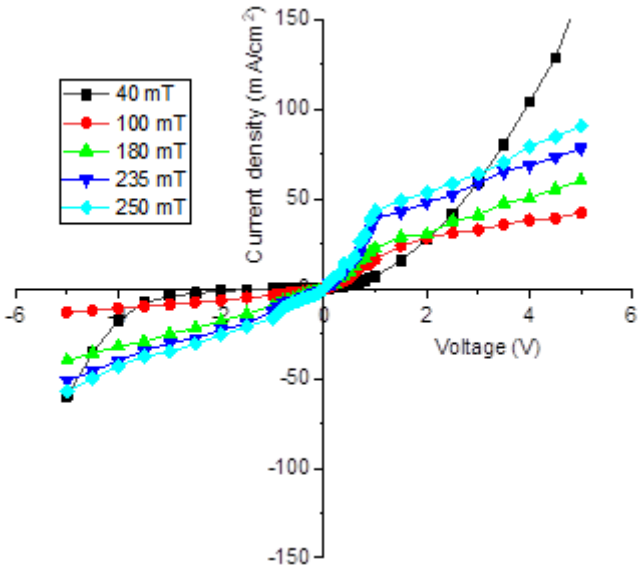

Figure 8: I-V characteristics of the Au:PbNPs/PS photodetector at the dark.

Table 3: Samples of Au:PbNPs/PS synthesized by 1020 mJ of laser light, their ideality factor, saturated current, and barrier height in different magnetic fields.

Magnetic field (mT)	**Slope**	n	**J_s (mA/cm^2)**	$\emptyset_{Bn}\ (eV)$
40	0.03112	1.20129	15.43	0.6715
100	0.03063	1.18246	23.8	0.6603
180	0.03014	1.16350	22.5	0.6617
235	0.02964	1.14415	39.1	0.6474
250	0.02913	1.12440	43.1	0.6449

Fig. 9 illustrates the effect of a magnetic field on the J-V characteristics of an Au:Pb NPs/PS heterojunction photodetector when subjected to light intensities of 30, 90, 158, 180, and 200 mW/cm^2. It was demonstrated that the formation of electron-hole pairs in the depletion zone and/or heterojunction's diffusion length boosts the current that passes through the photodetector when it is illuminated. Applying a magnetic field reduces the density of trap and interface states, contributing to the enhanced photocurrent by increasing the Au:Pb/PS surface area. Coating PS with Au:Pb NPs causes an increase in photocurrent at magnetic fields of 40, 100, 180, 235, and 250 mT.

The expected generation of electron-hole pairs within the photon energy depletion zone and the increasing reverse bias current are expected to be more than the smallest immediate band gap of a sandwich structure. As has been shown, the remarkable light sensitivity of these sandwich structures makes them a promising candidate for use in the development of optoelectronic devices. The gold standard for use in making optoelectronic sensors.

Fig.10 depicts how applying a magnetic field alters the Au spectral responsivity (R). The photodetector's responsivity was computed from:

$$R_\lambda = \frac{I_{ph}}{P} \qquad (4)$$

where: P is the light power at a specific wavelength and I_{ph} is Au:Pb NPs/PS photo-current detected at 450 and 600nm and absorption in the visible range, as well as 850 nm absorption in the near IR area.

Pb NPs/PS photodetectors were tested with a -5 V reverse voltage bias. With regard to all heterojunctions, response peaks were found at 450 nm, 600 nm, and 850 nm. The 450 nm peak may be attributed to Au:Pb core-shell's absorption edge, the 600 nm peak to the silicon substrate, and the 850 nm peak to the silicon substrate [42]. With the 250 mT magnetic field strength, the photodetector's maximum responsivity was 0.551 A/W at 650 nm. The final photodetector showed a small peak at 500nm, which might be a result of Au core's surface plasmon resonance effect. The fact that the shell thickens with the magnetic field could help explain why the photodetector is sensitive to magnetic fields; thicker shells are more sensitive.

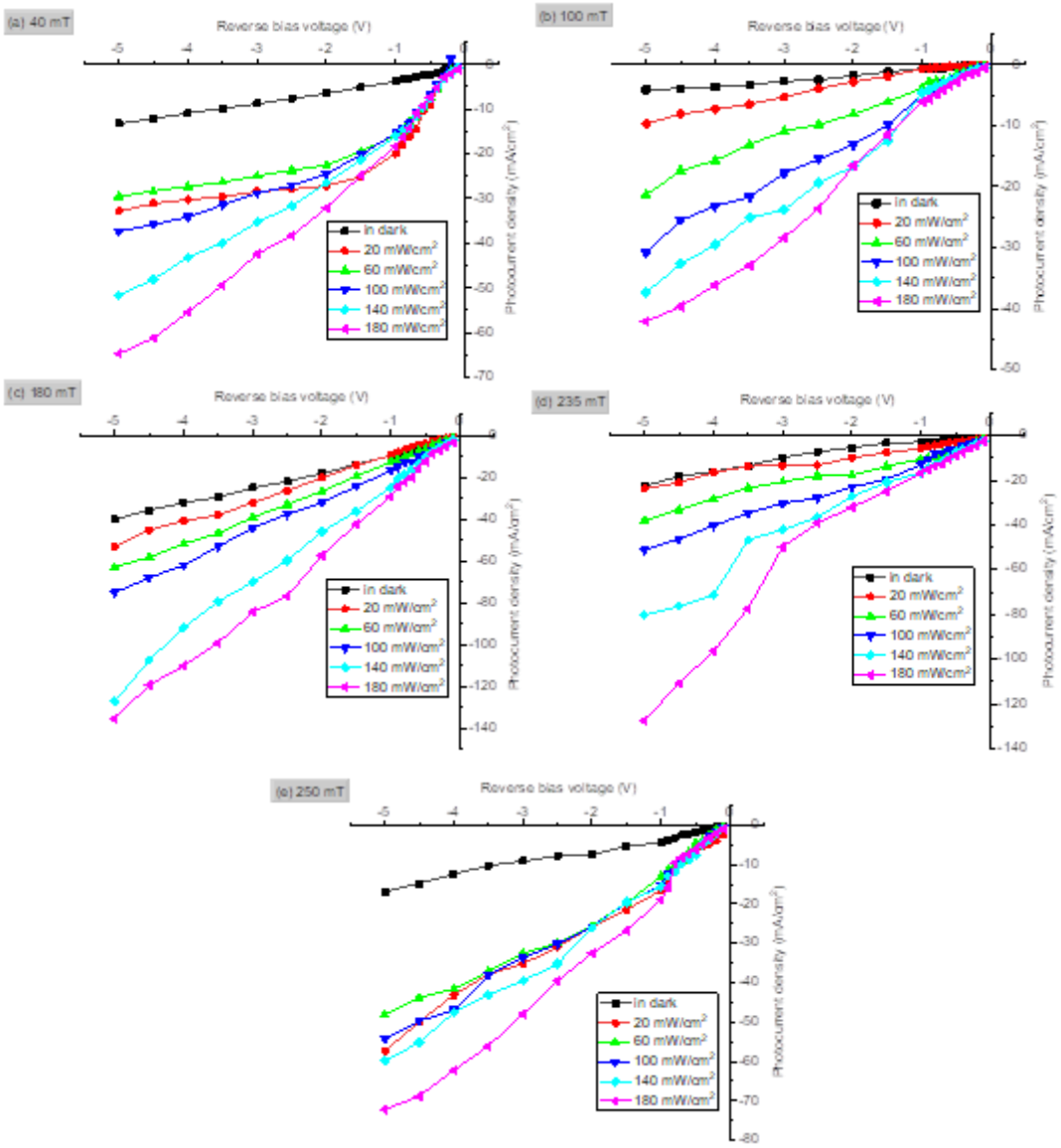

Figure 9: J–V curve of Au;Pb NPs/PS heterojunction photodetector manufactured at (a) B=40m, (b) B=100 mT, (c) B=180 mT, (d) B=235 mT and (e) B=250 mT illuminated at different light intensities.

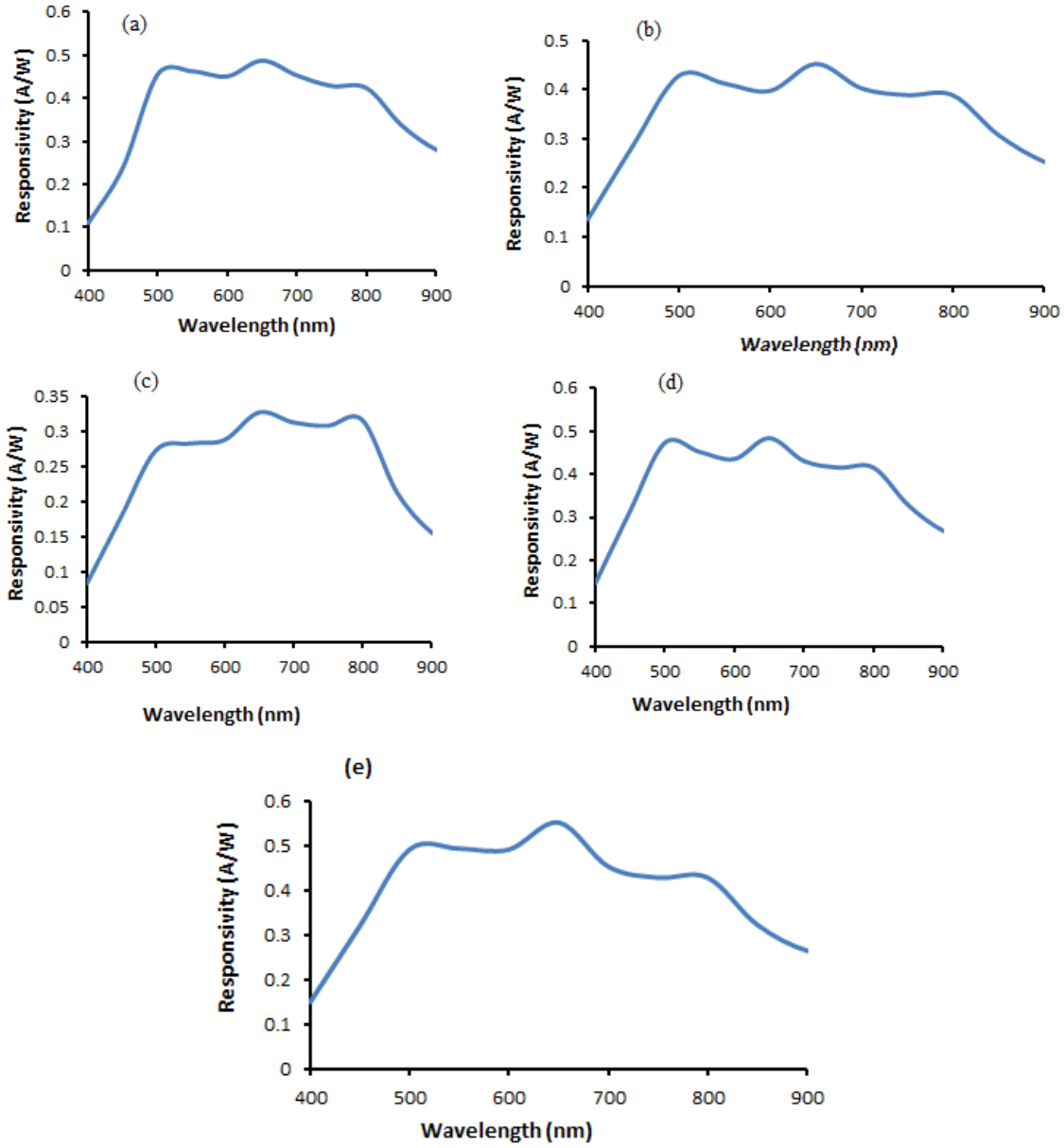

Figure 10: Responsivity of Au:Pb NPs/PS heterojunction photodetector manufactured with varied magnetic field strengths of (a)B=40mT, (b)B=100mT, (c)B=180mT, (d)B=235 mT, and (e)B=250mT.

Through raising the electrical resistance of NPs, the depletion area is brought closer to Au:Pb, improving short-wavelength responsiveness.

The photodetector's sensitivity was determined through calculating the detectivity (D*) of a photodetector utilized for defining frequency response (f =1/2$\pi\tau$) according to the following equation [43, 44]:

$$D^* = \sqrt{\frac{S_{det}\,\Delta f}{NEP}} \qquad (5)$$

where: (S_{det}) is the detector active area (S_{det}), and NEP is the noise equivalent power.

The results of a computation of photodetectors' specific detectivity D* as a function of magnetic fields are depicted in Fig. 11. An Au:Pb/PS heterojunction produced with a magnetic field of 250 mT achieved maximum D* values of 17.14 $\times 10^{12}$, 21.85$\times$ 10^{12} and 36.12$\times$ 10^{12} cm. $Hz^{1/2}$ /W at 450, 600, and 800 nm, respectively. A magnetic field must be present to maximize the photocurrent of the photodetector and reduce the electron-hole recombination produced by the generated high electric field region [45-47].

The quantum efficiency (QE) of a photodetector is defined as the ratio of incoming photons to electrons produced, as in the following equation: [48-50].

$$QE = \frac{h\upsilon}{q} R_\lambda \qquad (6)$$

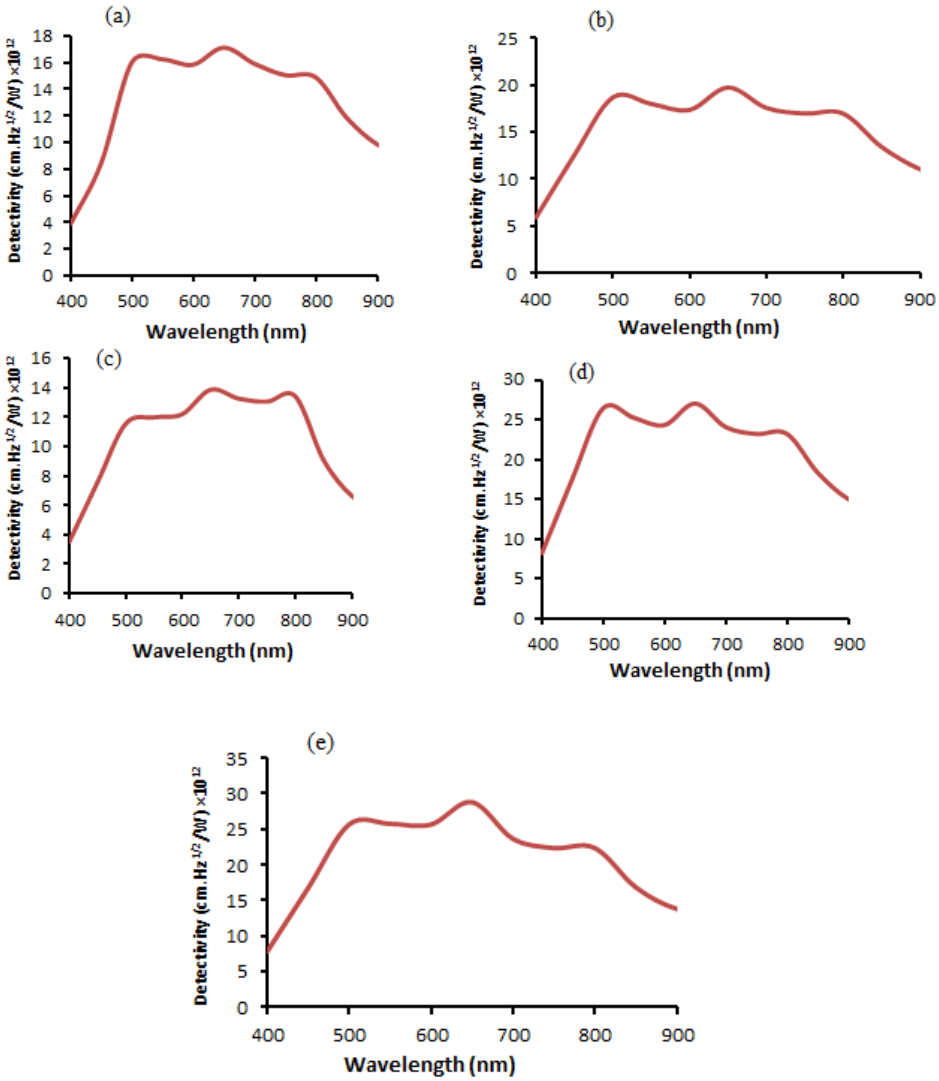

Figure 11: Detectivity of Au:Pb NPs/PS heterojunction photodetector manufactured with varied magnetic field strengths of :(a) B=40mT, (b) B=100mT, (c) B=180mT, (d) B=235 mT, and (e) B=250mT.

Fig.12 shows how the QE of a photodetector changes when subjected to a magnetic field. The photodetector's QE increased dramatically after being exposed to the magnetic field during production of the NPs. This enhancement may be due to the high surface area of the photodetector and the improved collecting efficiency of the generated carriers. By raising the magnetic field of the photodetector from 40-250mT, the photodetector's quantum efficiency was improved throughout production from (11.62 to 113.13) %. At 250 mT magnetic field, the 500 nm peak showed the maximum quantum efficiency of 113.13%. Quantum efficiency approaches 100% when bias voltage is raised because the deletion zone is larger.

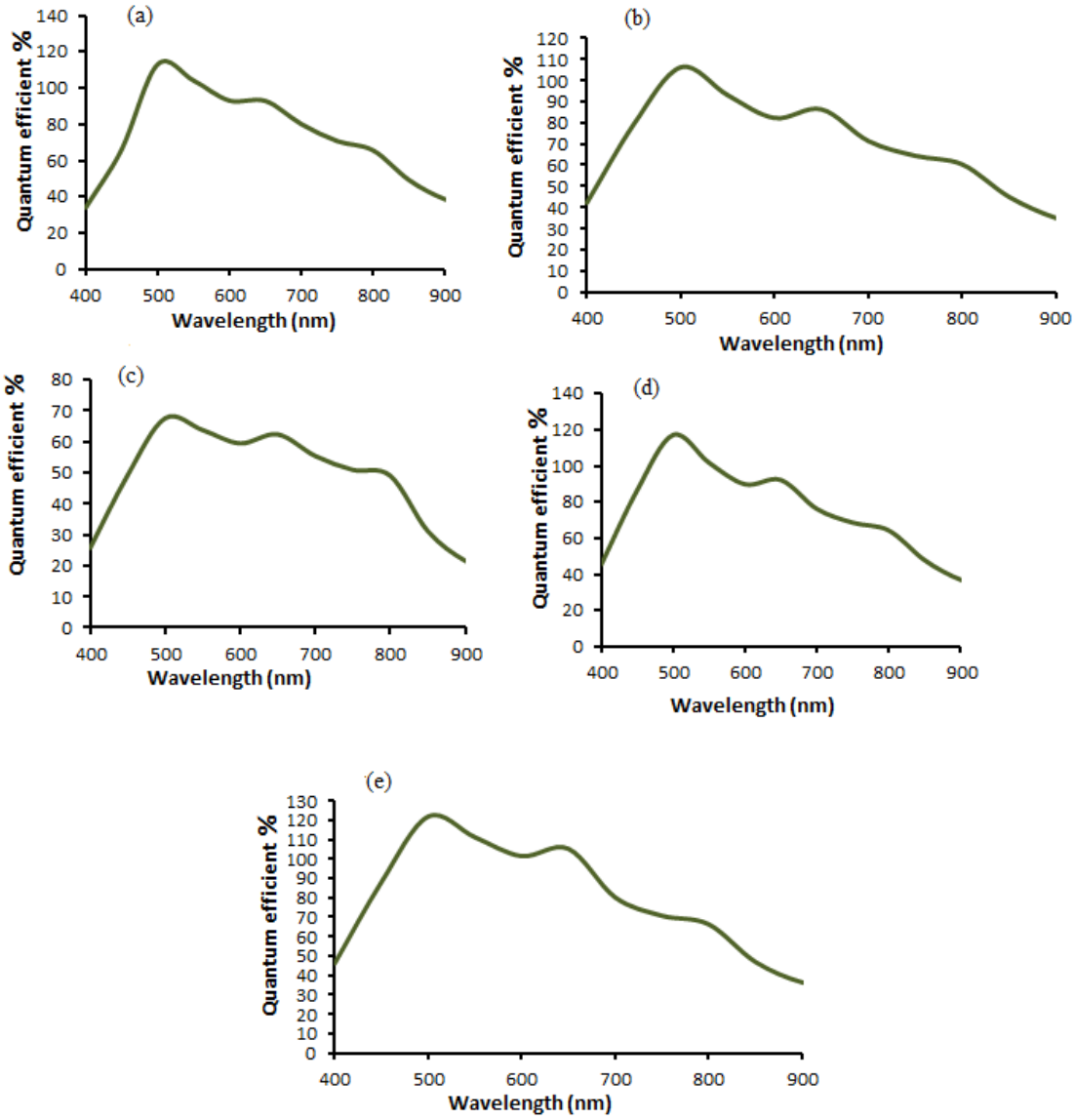

Figure 12: Quantum efficiency of Au:Pb NPs/PS heterojunction photodetector produced with varied magnetic field strengths:(a) B=40mT, (b) B=100mT, (c) B=180mT, (d) B=235 mT, and (e) B=250mT.

4. Conclusions

Au:PbNPs core/shell nanoparticles were synthesized in liquid in two steps using laser in the presence of a magnetic field. The magnetic field approach is a dependable method for enhancing and increasing the energy of laser shots used to ablate the bulk

material in order to produce NPs, and it is suggested as a means for obtaining smaller sized NPs. The effect of a 250mT magnetic field on the size distribution of Au:Pb produced by pulsed laser ablation in water was examined. The magnetic field was parallel to the surface of a submerged object and transverse to the direction of the laser beam incidence. Employing a magnetic field during laser ablation improved the characteristics of the Au:Pb NPs/PS heterojunction photodetector. The applied magnetic field during the laser ablation process is a positive factor in improving the volatility of SPR for Au:PbNPs. It enhanced all the parameters especially at 250 mT magnetic field strength. Based on the results, the Au:PbNPs/PS could potentially be recommended as a suitable material for a high photosensitivity Vis–NIR heterojunction photodetector.

Acknowledgements

The authors would like to thank the University of Baghdad, College of Science, Department of Physics, for their assistance in carrying out this work.

Conflict of interest

The authors declare that they have no conflict of interest.

References

1. F. A. Mutlak, R. K. Jamal, and A. F. Ahmed, Iraqi J. Sci. **62**, 517 (2021).
2. B. N. Chichkov, C. Momma, S. Nolte, F. Von Alvensleben, and A. Tünnermann, Appl. Phys. A **63**, 109 (1996).
3. D. Feldheim and C. Keating, Chem. Soci. Rev. **27**, 1 (1998).
4. D. I. Gittins, D. Bethell, D. J. Schiffrin, and R. J. Nichols, Nature **408**, 67 (2000).
5. N. Hanžić, T. Jurkin, A. Maksimović, and M. Gotić, Rad. Phys. Chem. **106**, 77 (2015).
6. M. A. Abed, F. A. Mutlak, A. F. Ahmed, U. M. Nayef, S. K. Abdulridha, and M. S. Jabir, Journal of Physics: Conference Series (IOP Publishing, 2021). p. 012013.
7. D. Boyer, P. Tamarat, A. Maali, B. Lounis, and M. Orrit, Science **297**, 1160 (2002).
8. D. Yelin, D. Oron, S. Thiberge, E. Moses, and Y. Silberberg, Opt. Exp. **11**, 1385 (2003).
9. M. Sainato, L. M. Strambini, S. Rella, E. Mazzotta, and G. Barillaro, ACS Appl. Mat. Inter. **7**, 7136 (2015).
10. A. F. Ahmed, M. R. Abdulameer, M. M. Kadhim, and F. A. Mutlak, Optik **249**, 168260 (2022).
11. L. He, Z. Jia, J. Zhou, H. Zhang, X. Lv, and D. Sun, Appl. Phys. B **123**, 1 (2017).
12. A. Sunatkari, S. Talwatkar, Y. Tamgadge, and G. Muley, Nanosci. Nanotechnol. **5**, 30 (2015).
13. M. Murawska, A. Skrzypczak, and M. Kozak, Act. Phys. Polo. A **121**, 888 (2012).
14. F. A. Mutlak, A. F. Ahmed, U. M. Nayef, Q. Al-Zaidi, and S. K. Abdulridha, Optik **237**, 166755 (2021).
15. Y.-J. Oh, J.-H. Kim, C. V. Thompson, and C. A. Ross, Nanoscale **5**, 401 (2013).
16. H. Krishna, N. Shirato, C. Favazza, and R. Kalyanaraman, J. Mat. Res. **26**, 154 (2011).
17. M. A. García, J. Phys. D: Appl. Phys. **44**, 283001 (2011).
18. B. Schneider, E. Dickinson, M. Vach, J. Hoijer, and L. Howard, Biosens. Bioelect. **15**, 597 (2000).
19. P. Sudeep, B. I. Ipe, K. G. Thomas, M. George, S. Barazzouk, S. Hotchandani, and P. V. Kamat, Nano Let. **2**, 29 (2002).
20. M.-C. Daniel and D. Astruc, Chem. Rev. **104**, 293 (2004).

21. M. A. Hayat, *Colloidal Gold: Principles, Methods, and Applications* (London, UK, Elsevier, 2012).
22. G. Compagnini, M. Fragal, L. D'urso, C. Spinella, and O. Puglisi, J. Mat. Res. **16**, 2934 (2001).
23. D. H. Jwied, U. M. Nayef, and F. A. Mutlak, Optik **239**, 166811 (2021).
24. N. R. Abdulhameed, H. A. Salih, K. I. Hassoon, and A. Ali, Eng. Technol. J. **32**, 1019 (2014).
25. X. Huang, X. Hu, S. Song, D. Mao, J. Lee, K. Koh, Z. Zhu, and H. Chen, Sensors Actuat. B: Chem. **305**, 127543 (2020).
26. K.-Y. Chan, D. Yang, B. Demir, A. P. Mouritz, H. Lin, B. Jia, and K.-T. Lau, Comp. Part B: Eng. **178**, 107480 (2019).
27. D. O. Idisi, H. Ali, J. Oke, S. Sarma, S. Moloi, S. C. Ray, H. Wang, N. R. Jana, W. Pong, and A. M. Strydom, Appl. Surf. Sci. **483**, 106 (2019).
28. S. Link and M. A. El-Sayed, Ann. Rev. Phys. Chem. **54**, 331 (2003).
29. R. He, X. Qian, J. Yin, and Z. Zhu, J. Mat. Chem. **12**, 3783 (2002).
30. R. Das, S. Nath, D. Chakdar, G. Gope, and R. Bhattacharjee, J Nanotech.. **5**, 1 (2009).
31. A. Taleb, C. Petit, and M. Pileni, J. Phys. Chem. B **102**, 2214 (1998).
32. M. Kim, S. Osone, T. Kim, H. Higashi, and T. Seto, KONA Powd. Part. J. **34**, 80 (2017).
33. D. H. Jwied, U. M. Nayef, and F. A. Mutlak, Optik **242**, 167207 (2021).
34. M. Sonmez and R. Kumar, Hydrometallurgy **95**, 53 (2009).
35. B. Šljukić, C. E. Banks, A. Crossley, and R. G. Compton, Analyt. Chim. Act. **587**, 240 (2007).
36. W. H. Dumbaugh and J. C. Lapp, J. American Ceram. Soci. **75**, 2315 (1992).
37. A. Amiri, M. Mohammadi, and M. Shabani, Elect. J. Bio. **12**, 110 (2016).
38. J. Xiao, P. Liu, C. X. Wang, and G. W. Yang, Prog. Mat. Sci. **87**, 140 (2017).
39. S. S. Shaker, R. A. Ismail, and D. S. Ahmed, Silicon **14**, 107 (2022).
40. A. S. Alber and F. A. Mutlak, J. Opt. **52**, 1477 (2023).
41. A. J. Jwar, U. M. Nayef, and F. A. Mutlak, Plasmonics **18**, 595 (2023).
42. F. A. Mutlak, Turkish J. Phys. **38**, 130 (2014).
43. N. H. Harb and F. A. Mutlak, Optik **249**, 168298 (2022).
44. S. S. Khudiar, U. M. Nayef, and F. A. Mutlak, Optik **244**, 167530 (2021).
45. A. S. Alber and F. A. Mutlak, Optik **265**, 169427 (2022).
46. D. H. Jwied, U. M. Nayef, and F. A. Mutlak, Optik **241**, 167013 (2021).
47. A. F. Ahmed, W. I. Yaseen, Q. A. Abbas, and F. A. Mutlak, Appl. Phys. A **127**, 1 (2021).
48. H. N. Abid, U. M. Nayef, F. A. Mutlak, and I. M. Khudhair, Iraqi J. Phys. **16**, 162 (2018).
49. N. H. Harb and F. A. Mutlak, Optik **246**, 167800 (2021).
50. M. A. Khalaf, B. M. Ahmed, and K. A. Aadim, Iraqi J. Sci. **61**, 1665 (2020).

الاستئصال بالليزر بخطوتين للتوليف لأنشاء Au:Pb core/shell ككاشف ضوئي متغاير عالي الأداء قائم على السيليكون

زينة علاء عبد الحميد[1] وفلاح عبد الحسن مطلك[1]
[1]قسم الفيزياء، كلية العلوم، جامعة بغداد، بغداد، العراق

الخلاصة

في هذا العمل، تم تصنيع جسيمات الذهب الغروية/الرصاص (Au:Pb) النانوية الأساسية/القشرية في سائل عند 532 نانومتر باستخدام طريقة الاستئصال بالليزر. أثر التحقيق في المجال المغناطيسي الخارجي أثناء عملية الاستئصال بالليزر على خصائص قلب وقذيفة Au:Pb NP. يعزز المجال المغناطيسي تبلور القشرة الأساسية. زادت طاقة فجوة النطاق البصري من 2.067 إلى 2.086 فولت في وجود المجال المغناطيسي. كما أدى إلى زيادة التركيز وانخفاض حجم الجسيمات النانوية مما أدى إلى زيادة الامتصاصية. أدت قوة المجال المغناطيسي التي تبلغ 250 طن متري إلى زيادة كفاءة الإزالة. أدى المجال المغناطيسي الخارجي إلى تقليل تكتل وتجميع الجسيمات النانويه بشكل كبير. لقد أنشأنا وميزنا كاشف ضوئي متغاير الوصلات Au:Pb/السيليكون المسامي (PS). وقد عزز المجال المغناطيسي خصائصه بشكل كبير. زادت استجابة (R lect) للكاشف الضوئي من 0.093 إلى 0.551 A / W عند 650 = 650 نانومتر عن طريق زيادة المجال المغناطيسي. من ناحية أخرى، تتمتع مادة Au:Pb/PS النهائية بأفضل استقرار للتيار الضوئي، مما يدل على أن إضافة Au:Pb NPs يمكن أن تجعل الخصائص الكهربائية الضوئية لـ PS أكثر استقرارًا. في النهاية، أظهرت نتائج الكاشف الضوئي المتغاير Au:Pb NPs/PS أن معلمات الكاشف الضوئي أصبحت أفضل بكثير عند وجود مجال مغناطيسي. من خلال تغيير ظروف التحضير، يمكننا إنتاج أجهزة كهروضوئية أساسية/قشرية عالية الأداء.

الكلمات المفتاحية: السيليكون النانوي، الحفر الكهروكيميائي، الذهب:الرصاص النانوي، الاستئصال بالليزر، الكواشف الضوئية.